Ultralong-recovery-time nanosecond electroporation system enabled by orientational-disordering processes

Denise Lee,[1] J Shamita Naikar,[2] Sophia S. Y. Chan,[1] Maria Prisca Meivita,[1] Lunna Li,[1] Yaw Sing Tan,[3] Natasa Bajalovic,[1,*] Desmond K. Loke[1,2,*]

[1]*Department of Science, Mathematics and Technology, Singapore University of Technology and Design, Singapore 487372, Singapore*

[2]*Office of Innovation, Changi General Hospital, Singapore, 529889, Singapore*

[3]*Bioinformatics Institute, Agency for Science, Technology and Research (A*STAR), Singapore 138671, Singapore*

[*]*Correspondence and requests for materials should be addressed to N.B. (email: natasa_bajalovic@sutd.edu.sg) or D.K.L. (email: desmond_loke@sutd.edu.sg)*

Abstract

The growing importance of applications based on molecular medicine and genetic engineering is driving the need to develop high-performance electroporation technologies. Electroporation phenomenon involves disruption of the cell for increasing membrane permeability. Although there is a multitude of research focused on exploring new electroporation techniques, the engineering of programming schemes suitable for these electroporation methods remain a challenge. Nanosecond stimulations could be promising candidates for these schemes thanks to their ability to generate a wide range of biological responses. Here we control the membrane permeabilization of cancer cells using different number of electric-field pulses through orientational disordering effects. We then report our exploration of few-volt nanosecond alternating-current (AC) stimulation with increased number of pulses for developing electroporation systems. A recovery time of ~720 min was achieved, which is above the average of ~76 min for existing electroporation methods using medium cell populations, as well as previously unreported increased conductance with an increase in number of pulses using weak bias-amplitudes. All-atom molecular dynamics simulations reveal the orientation-disordering-facilitated increase in degree of permeabilization. These findings highlight the potential of few-volt-nanosecond-AC-stimulation-with-increased-number-of-pulse strategies for the development of next-generation low-power electroporation systems.

1. Introduction

Emerging and critical applications in fields, including genetic engineering, molecular medicine and gene therapy require high-performance electroporation techniques for operations, such as food sterilization,[1] genetic payload transfer,[2] tumor ablation[3, 4] and cell monitoring.[5, 6] Next-generation electroporation techniques have therefore been an important subject of research. Moreover, some of the electroporation devices have made inroads into Covid-19 vaccine technologies.[7] Electroporation phenomenon, based on disruption of the cell, showing increased membrane permeability, allows molecular and ionic diffusion across the cell membrane. The transitory increase in membrane permeability is harnessed in electroporation technologies including electrochemotherapy,[8, 9] electrofusion[10] and gene transfection.[11, 12] On the other hand, irreversible electroporation results in cell death via a loss of homeostasis for nonthermal cancer cell ablation.[13, 14] The success of this approach depends on identifying an ideal programming strategy capable of harnessing the full potential of this technique.

Nanosecond electrical stimulation is a promising candidate for realizing next-generation electroporation techniques. Nanosecond stimulation can generate a wide range of biological responses, such as the permeabilization of intracellular organelles[15], calcium bursts[16–18], apoptosis pathway activation[19, 20], phosphatidylserine translocation[21] and formation of long-lived nanopores.[22] As a result, nanosecond stimulations have been harnessed as a tool for understanding behavior of cancerous cells. Nanosecond stimulations have been demonstrated to generate nanopores with a diameter of 1 – 1.5 nm.[23–25] These nanopores were long-lived, and they remained open several minutes after applying the nanosecond stimulations.[26] Moreover, experiments have demonstrated that the nanopore resealing/ membrane repair process can be

controlled by Annexin V genes in Hela cells, which indicates that nanopore resealing involves active biological processes.[27]

Recent research advances have been focused on nanostructure-enhanced electroporation to reduce the bias-voltage applied and decrease heat-induced cell damage. Nanostructure-facilitated electroporation could enhance the intensity of localized electric field, decreasing the applied bias-voltage and its accompanying damage to cells.[28, 29] In contrast, conventional bulk electroporation may utilize electric fields in the several thousand volts per centimeter range. Moreover, nanostructures such as nanostraws, nanoneedles and nanowires have been integrated into systems to realize localized electroporation for intracellular drug delivery.[30, 31]

Recently, experiments have focused on the biological aftermath of electroporation techniques. Experiments have shown when a shortened bias pulse is applied to cells, the systems exhibit a longer recovery time.[32–34] Although the hydrophilic pores, electrically-altered lipids and modulated-voltage-gated ion channels increase membrane permeability within microseconds upon the application of strong electric-fields, the mechanism and timescale (from minutes to hours) of membrane resealing after applying nanosecond stimulations is still not well understood. Furthermore, the nanopores can exhibit complex behaviors, such as current/ voltage sensitivity and ion selectivity. Moreover, the disruption of cell cytoskeleton caused by pulsed electric fields has been explored.[35–37] As the cytoskeleton is dynamically connected to the cell membrane,[38–40] the membrane permeability after electroporation and cell viability can be modified by the chemical or physical disruption of cytoskeleton.[36, 41] Furthermore, the elastic modulus of cells decreases after applying electric fields.[41–43] Thus, our interest is in understanding membrane permeabilization upon the application of nanosecond stimulations.

In this work, we demonstrate that by modulating the membrane permeabilization process, we can alter the degree of permeabilization of cancer cells by programming means. We then show the utilization of few-volt nanosecond (AC) stimulation with increased number of pulses for electroporation and demonstrate low-power electroporation systems. A recovery time of ~720 min was achieved, which is above an average of ~76 min for existing electroporation methods using medium cell populations, which allows cells to be monitored for longer times for substantially enhancing monitoring reliability. A previously unreported increased conductance with an increase in number of AC pulses using weak bias amplitudes was also achieved, which enables the control of electrical signatures of cells with weaker bias-voltages for enhancing monitoring safety. All-atom molecular dynamics simulations reveal the orientational-disordering-facilitated increase in degree of permeabilization. These suggest targeted opportunities to optimize electroporation for genetic engineering, molecular medicine and gene therapy.

Methods

MD simulations setup and parameters. The lipid bilayer model was generated using CHARMM-GUI.[44, 45] Its composition was based on the representative cancer bilayer membrane model used by Klahn and Zacharias.[46, 47] The ratio of the lipids were kept the same but the membrane model was scaled by a factor of two, four and five in order to better observe the effects of electroporation on the membrane. The membrane model consists of 400/ 800/ 1000 lipids in the inner leaflet and 400/ 800/ 1000 lipids in the outer leaflet (we call it the 800/ 1600/ 2000-lipid bilayer model), including 1-palmitoyl-2-oleoyl-sn-glycero-3-phosphocholine (POPC), 1-palmatoyl-2-oleoyl-sn-glycero-3-phosphoethanolamine (POPE), 1-palmitoyl-2-oleoyl-sn-glycero-3-phospho-L-serine (POPS), palmitoylsphingomyelin (SM16) and cholesterol (CHOL) (Supporting Table S1). The lipid bilayer was set up along the *x*–*y* plane, with the *z*–axis passing through the bilayer normal. The simulation box included the lipid bilayer surrounded by TIP3P water molecules, 0.15 M NaCl and sodium counterions.[48]

For each of the lipid bilayer systems, two independent MD simulation runs were performed with different initial atomic velocities and a time step of 2 fs using the Leap-Frog integrator. MD simulations were performed with GROMACS 2020.4 using the Slipids force field.[49–51] The cancerous lipid bilayer model was subjected to energy minimization with the steepest descent algorithm for ~5000 steps, and then equilibrated for 100 ps in the isochoric-isothermal (NVT) ensemble. The temperature of the system was kept constant at 300 K with a coupling constant of 0.1 ps using the velocity-rescaling thermostat.[52] The second equilibration step was performed in the isothermal-isobaric (NPT) ensemble for another 1 ns, with the pressure being maintained at 1

bar via the Parrinello-Rahmen barostat.[53] Semi-isotropic coupling scheme was executed using the Nosé–Hoover thermostat to keep the temperature constant.[54, 55]

The production run was carried out at constant temperature (300 K) and pressure (1 bar) for 100 ns during which two electric-field pulses of 0.25 V/nm were applied at 50 and 51.2 ns, each for 0.6 ns. Coordinates of all atoms were saved every 20 ps. The van der Waals interactions were calculated with a cut-off distance of 1 nm and all long-range electrostatic interactions were treated with the particle-mesh Ewald scheme.[56, 57] The SETTLE algorithm was used to constrain the bonds in the water molecules.[58] Lipid bonds were constrained by the LINCS algorithm.[59]

Data Analysis The snapshots of models were generated and the pore diameters were analyzed using the Visual Molecular Dynamics (VMD) software.[60] The surface area per lipid of the model after applying the first and second electric-field pulses was analyzed using the GridMAT-MD tool.[61] The angle distribution of phosphorous-nitrogen headgroup (PN) vectors was calculated using the *gmx gangle* utility,[62] which computes the angles between PN vectors and bilayer normal (*z*–axis). The deuterium order parameters of the model were determined using the *gmx order* tool.[63]

Cell line and cell culture. PANC-1 cell line was purchased from American Type Culture Collection (ATCC). Cell culture was performed in Dulbecco's modified eagle's medium (DMEM) supplemented with 10% fetal bovine serum (FBS) and 1% L-glutamine. Cells were incubated at 37 °C in a humidified incubator with an atmosphere of 5% CO_2.

Cell viability studies. PANC-1 cells were plated at a cell density of 5×10^3 cells per well and incubated 24 h prior to experiments. Cells were electroporated with different number of pulses and incubated 24 h or 48 h after electrical stimulation. Cell viability studies were determined through WST-1 assays according to the protocol of manufacturer and the absorbance of cells was measured at $\lambda = 450$ nm.

Experimental setup and cell viability studies. Sterilization of ITO subsystems were performed with 70% ethanol and exposure to ultra-violet (UV) irradiation. PANC-1 cells were plated on ITO subsystems at a seeding density of 5×10^3 cells per well and incubated for 24 h prior to each experiment.

Electrical setup and electroporation protocol. Prior to electrical experiments, cells were washed with Dulbecco's phosphate buffered saline (DPBS) and fresh DMEM was added. The experiments were performed with 5 V pulses and using different number of pulses in the 0 – 500 pulses range. The impedance was recorded at different time intervals of 0, 5, 10, 15, 60, 120, 360 and 720 min.

Different number of pulses or bias voltages were programmed using an arbitrary waveform generator (Tektronix). The pulses were administered to the cells via external circuitry and the signals passing through the cells at various time intervals were recorded with an oscilloscope (Tektronix). The cell impedance R_{cell} was calculated by Eqs. S1 and S2

$$I = \frac{V_{\text{out}}}{R_3} \tag{S1}$$

$$R_{\text{cell}} = \frac{V_{\text{in}} - V_{\text{out}}}{I} - R_2 \quad \text{(S2)}$$

Normalized cell impedance was computed using ratio of the impedance of system with specified number of pulses to impedance of pure system (0 pulse).

Results

All-atom MD simulations. Atomistic molecular dynamics (MD) simulations were performed to understand membrane permeabilization upon applying electrical stimulations. We built the lipid-bilayer models based on the models utilized by Klähn *et al.*[47] (Supporting Table S1), which incorporate both the natural asymmetries and multiplexed compositions of cancer cell membranes. Bilayer models with 400 lipids showing excellent results have been demonstrated in simulations.[47] We chose to utilize a larger lipid-bilayer model to accommodate the formation of multiple pores. However, as the model size increases, the simulations become slower. The simulations become computationally demanding when bilayer models with 1600 lipids were used. Based on these computation initiatives and constraints, we chose to harness a 1600-lipid bilayer model. Two simulation runs were performed, and the models were stimulated with two electric-field pulses. Schematic illustration of the pulse waveform is shown in Fig. 1a. Figures 1b–d shows snapshots of the model after applying the first and second electric-field pulses. The pore population of the model upon application of the first electric-field pulse is larger than that of the pristine model, indicating a larger degree of membrane permeabilization. This behavior is consistent with that of previous calculations of lipid-bilayer models with constant electric-fields.[6, 64, 65] We found that by comparison with the model after injecting the first electric-field pulse, the model after applying the second electric-field pulse exhibits a larger degree of membrane permeabilization, as indicated by a larger pore population (Figs. 1e, f). This is further supported by the calculation of surface area per lipid, which describes the amount of space available to each lipid moving around the surface of lipid-bilayer-models. The model upon applying the second electric-field pulse shows

a larger area per lipid compared to that of the model upon injection of the first electric-field pulse, indicating a larger degree of membrane permeabilization (Fig. 1g, Supporting Fig. S1).

These results indicate that the degree of membrane permeabilization can be altered by the number of electric-field pulses. For the cell membrane, electrical properties are dominated by the structure and composition of lipid bilayers.[66] When a strong electrical stimulus is applied to the membrane, the membrane is shorted (becomes a short circuit) due to the dielectric breakdown in membranes.[67, 68] As a result, the lipid bilayer becomes electrically conductive, which leads to a small impedance.[69] Moreover, the application of multiple stimuli causes a larger degree of dielectric breakdown due to the generation of a higher population of pores.[26] Thus, the lipid bilayer becomes more conductive, resulting in a decrease in impedance.

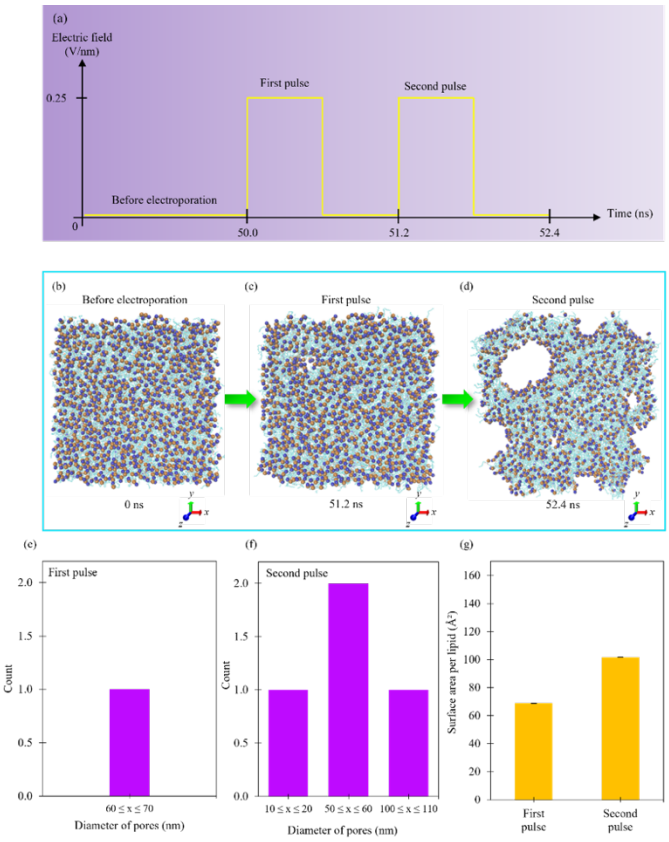

Figure 1. All-atom MD simulations. **a)** Schematic illustration of the electric-field pulse waveform utilized in the simulations. **b–d)** Snapshots of the 1600-lipid bilayer model viewed from the top after 0 ns, 51.2 ns and 52.4 ns of simulations. The electric-field and pulse length were set at 0.25 V/nm and 0.6 ns, respectively. Color coding of the atoms: P, blue; N, orange. Lipid tails are depicted in cyan. **e, f)** Pore distributions of the 1600-lipid bilayer model after applying the **e)** first and **f)** second electric-field pulses (upon 51.2 ns and 52.4 ns of simulations). **g)** The surface-area-per-lipid of the 1600-lipid bilayer model upon application of the first and second electric-field pulses. The error bars show the range of values obtained from simulations performed upon the application of electric-field pulses (after first pulse, 50.6–51.2 ns; following second pulse, 51.8–52.4 ns). The results for the 800- and 2000-lipid bilayer models can be found in Supporting Fig. S1.

Further analyses of the model were performed to obtain deeper insights into the membrane permeabilization process after electrical stimulations. We analyzed the headgroup tilts of phospholipids in lipid-bilayer models, which describes the responses of headgroups to electrical stimulations (Fig. 2a).[70, 71] The headgroup tilt is defined as the angle of vector passing through the phosphorous/ nitrogen (PN) atoms relative to normal of the lipid bilayer (z–axis). We call this vector 'PN vector'. Figure 2b, c show the PN-vector-angle distributions of models with different number of electric-field pulses. A peak at 90˚ is observed in the unperturbed lipid bilayer model. The peak of the PN-vector-angle distribution shifts to larger angles (from 90˚ to 100˚) after applying the first electric-field pulse, indicating that the phospholipid headgroups are aligned more parallel to normal of the bilayer model. This corresponds to a small change in degree of membrane permeabilization. Moreover, we find that the PN-vector-angle-distribution peak broadens after injecting the second electric-field pulse. Furthermore, a larger shift in the peak of the PN-vector-angle distribution (from 90˚ to 110˚ – 155˚) is observed. These indicate that the majority of phospholipid headgroups are aligned almost parallel to normal of the lipid-bilayer, corresponding to a large change in degree of membrane permeabilization.

Moreover, we investigated the orientational order of membranes using the deuterium-order parameter. The deuterium-order parameter of a membrane can be described by

$$S_{CD} = \frac{1}{2}\langle 3\,cos^2\,\theta - 1\rangle \tag{1}$$

where θ is the angle between the C–H bond vector in hydrocarbon chain (Fig. 2d) and normal of the lipid bilayer (z–axis).[72, 73] The deuterium-order parameter characterizes the fluidity and tension of membranes.[72, 73] A decrease in this parameter corresponds to an increased fluidity of membranes and subsequent decreasing tension in membranes.[72, 73] Close to the edge of the

membrane, the degree of orientational order of the lipid-tail carbon atoms is small. The degree of orientational order increases and then decreases as the chain extends into center-of-membrane.[73] Figure 2e, f and Supporting Fig. S2 show the deuterium order parameters for different phospholipid species. Orientational order analysis shows that the deuterium-order parameters of *sn*-1 chains of phospholipids POPC and POPE decrease on application of the second electric-field pulse compared to the first electric-field pulse (average decrease of ~40% for both POPC sn-1 and POPE sn-1) (Figs. 2e, f), indicating a decrease in membrane tension.

Experiments and theoretical studies have demonstrated that a decrease in membrane tension results in an increased pore-resealing time.[76, 77] For instance, Zhelev *et al.* demonstrated the possibility of tuning pore lifetimes through adjustments in the membrane tension, which allow the pores to remain open for a long time.[76] In another instance, Karatekin *et al.* have shown how surfactants can decrease membrane tension in giant unilamellar vesicles, increasing the lifespan of pores generated through electroporation.[77] Modelling studies have further shown that pore resealing is dominated by the tension of pore lines,[77] where opening of pores relaxes the surface tension of membranes.[78] This increases the energy barrier for pore closure, resulting in long-lived pores that stay for an extended period of time.[79] These simulations suggest that the administration of increased number of electric-field pulses decreases membrane tension, which may lead to an increase in pore-recovery times.

Additionally, we investigated the isothermal-membrane-area-compressibility modulus (K_A) of lipid-bilayer models (Supporting Fig. S3). This parameter describes the resistance of membranes to isotropic stress and can be represented by

$$K_A = \frac{AK_BT}{{\sigma_A}^2} \tag{2}$$

where A is the average total area of membranes, K_B is the Boltzmann's constant, T is the temperature and ${\sigma_A}^2$ is the standard deviation of area-per-lipid in membranes. We further find that the K_A decreases by ~88.3% on application of the second electric-field pulse compared to the first electric pulse (Supporting Fig. S3b), indicating a decreased resistance of the membrane to isotropic stress.

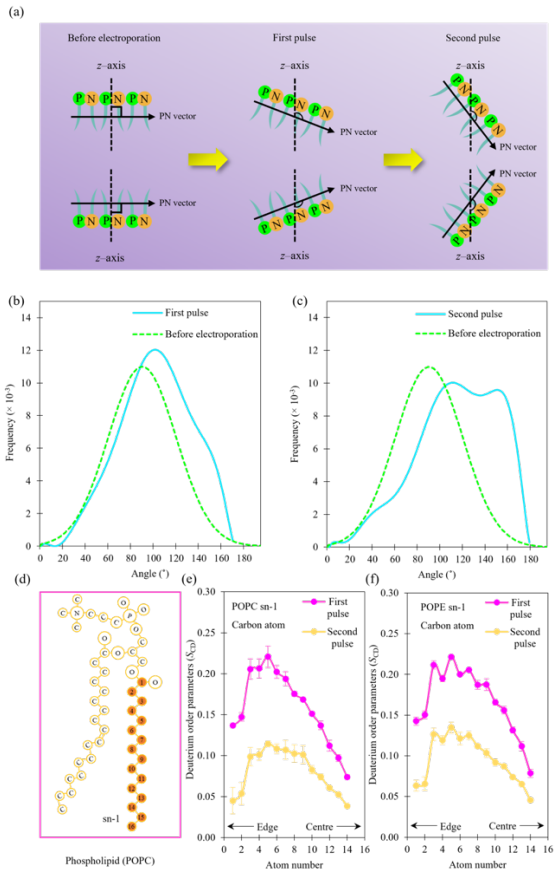

Figure 2. PN-vector-angle-distribution and deuterium-order-parameter analyses of the lipid bilayer model. a) Schematic illustration of the variations in phosphorous/ nitrogen (PN) vector angles upon administering the first and second electric-field pulses. **b, c)** PN-vector-angle distributions of the 1600-lipid bilayer model upon application of the **b)** first and **c)** second electric-field pulses (following 51.2 ns and 52.4 ns of simulations). **d)** Schematic illustration of the numbers assigned to the carbon atoms in a representative phospholipid (POPC) molecule. **e, f)** Deuterium order parameters of the sn-1 chains of **e)** POPC and **f)** POPE in the 1600-lipid bilayer model after injecting the first and second electric-field pulses (thereupon 51.2 ns and 52.4 ns of simulations). The error bars show the range of values obtained from simulations performed for two different runs. The results for the 800- and 2000-lipid bilayer models can be found in Supporting Fig. S2.

Cancer cell monitoring performance of few-volt nanosecond AC electroporation system with increased number of pulses. Motivated by the theoretical findings, we developed a few-volt nanosecond AC electroporation system with increasing number of pulses and performed electrical characterization of pancreatic cancer cells (PANC-l). We fabricated the electroporation system with a lateral-type structure (Fig. 3a). Glass was used as the starting material, on which the ~650 nm-thick left and right indium tin oxide (ITO) electrodes were deposited for connecting the system to external circuitries. The distance between the electrodes was chosen to be ~100 μm. Finally, the PANC-l cells were plated to complete the system. We administered 5 V, 100 ns pulses to PANC-1 cells. The electric-field was calculated to be ~500 V/cm ($E = V/ d$ = 5 V/ 100 μm = 500 V/cm, where V is the bias-voltage and d is the distance between the electrodes). Different number of pulses in the 10 – 200 pulses range was utilized (Fig. 3b). We investigated impedance of the system upon application of the AC pulses. The PANC-l cells remained viable 24 h and 48 h after injecting the AC pulses (0 – 500 pulses) (Supporting Fig. S4). This indicates that the cells have recovered by 24 h, and that changes in the impedance after application of the pulses were not due to cell death.

We investigated time evolution of average normalized impedance of the system after applying the AC pulses (Fig. 3c). The ratio of sum of normalized impedance for n different systems to the number of systems n is utilized to describe the average normalized impedance. Impedance measurements can be utilized to determine the permeability of cell membranes after electroporation.[80] The impedance response upon application of the AC pulses is shown in Fig. 3c. We observed two different recovery regions depending on the membrane permeabilization process: 1) region I (0 to 15 min) and 2) region II (15 to 360 min). In region I, we observe a

decrease in average normalized impedance of the system after application of the AC pulses, i.e., at $t = 0$, by ~15% – 20% compared to that of control system (cells only) (from 1.00 to 0.80–0.88). We call the average normalized impedance of the system upon applying the AC pulses at $t = 0$ the initial average normalized impedance (0.80–0.88). Over the 0–5 min time-period, the average normalized impedance of the system after the application of AC pulses decreases to 75% – 80% of the initial average normalized impedance (from 0.80–0.88 to 0.58–0.70). The average normalized impedance then recovers to 87% – 98% of initial-average-normalized-impedance during the 5–15 min time-period (from 0.58–0.70 to 0.72–0.82). In region II, through the 15–360 min time-period, a further recovery of the average normalized impedance to 93% – 100% of initial average normalized impedance (from 0.72–0.82 to 0.78–0.84) is observed. The system shows a recovery time of ~360 min. Besides, Pavlin *et al.* have suggested that when multiple pulses are applied, a subpopulation of pores generated during electroporation can transform into metastable pores.[81] Additionally, they showed that the percentage of long-lived pores formed increases with increasing number of pulses.[81] In this work, when a large number of pulses (500 pulses) are injected, the system further exhibits a long recovery time of ~720 min (Supporting Fig. S5), which is above an average of ~76 min for current electroporation methods using medium cell populations (Supporting Fig. S6). Furthermore, the system exhibits an increased average normalized impedance when the pulse type is changed from the square-based pulse to triangular-/ sawtooth-based pulse, indicating that the degree of membrane permeability alters for different electrical-stimulation types (Supporting Fig. S7).

Figure 3d further shows the normalized impedance of PANC-1 cells 5 min after application of the AC pulses. When compared to control system (cells only) (1.00), normalized impedance of the system after applying 10 and 200 pulses decrease by ~30% (0.70) and ~35% (0.65),

respectively. This indicates that an increased number of pulses can lead to a larger degree of membrane permeabilization, which agrees well with the results of MD-simulations.

Notably, the few-volt nanosecond AC-stimulation system with an increased number of pulses not only demonstrates a long recovery time, but also increasing conductance with an increase in the number of pulses via weak-bias amplitudes, and also excellent cell viability for a large number of pulses. Moreover, atomistic MD simulations reveal the orientational-disordering-facilitated increase in degree of permeabilization, as well as phospholipid headgroup flexibility after applying electric-field pulses, along with the utilization of a large lipid-bilayer model. These highlight the potential of a combined experimental atomistic approach to demonstrate long recovery times in addition to elucidating membrane-permeabilization kinetics.

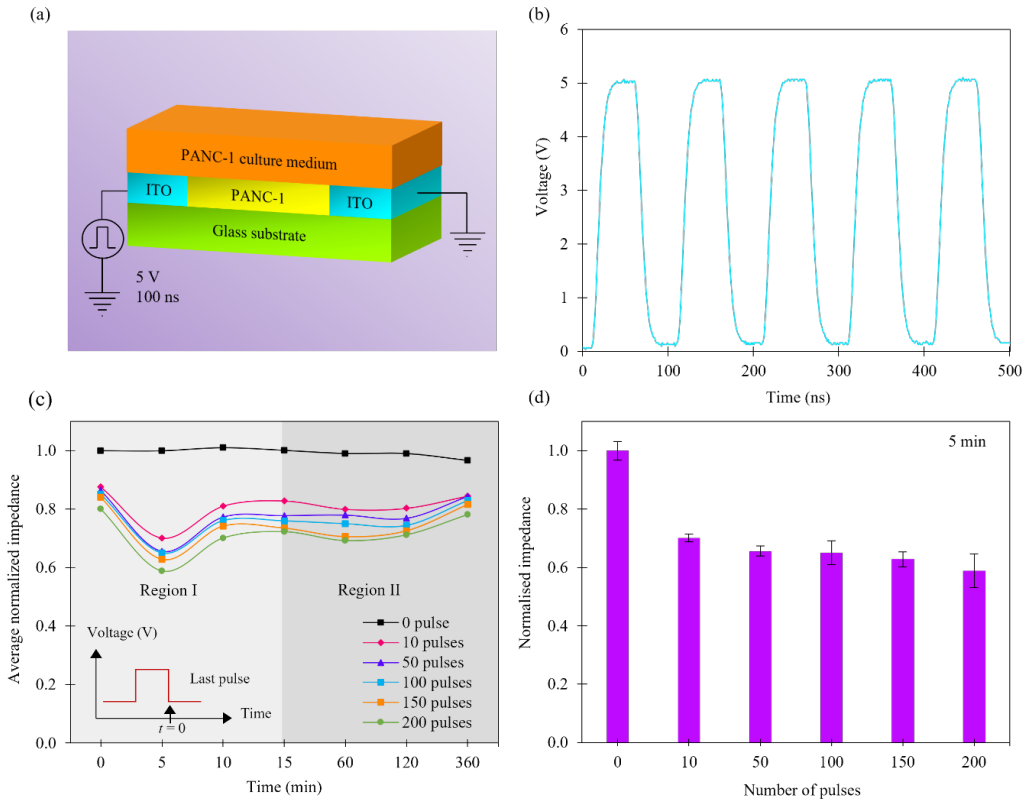

Figure 3. Response of the cancer cell system exposed to few-volt nanosecond AC stimulation with increased number of pulses. a) Schematic illustration of the system structure utilized. **b)** Waveform of the AC pulses administered to the cells. The bias amplitude and pulse length were set to 5 V and 100 ns, respectively. Different number of pulses in the 0 – 200 pulses range were utilized. **c)** Time evolution of average normalized impedance of the system upon application of different number of pulses. The average normalized impedance is computed through the ratio of sum of normalized impedance for n different systems to the number of systems n (n = 6). The significance can be found in Supporting Table S2. **d)** Normalized impedance of the system 5 min after the AC stimulation for different number of pulses. The error bars show the range of values obtained from experiments performed on 6 different systems. The significance can be found in Supporting Table S2.

Discussion

Experiments have demonstrated that nanosecond stimulations result in the formation of long-lived nanopores.[22, 26, 78, 81] However, traditional studies on pore lifetimes may not be established in literature because the nanopores generated might not be consistent in size and are too small to be measured using conventional fluorescence imaging.[82] Although ions can be utilized as electroporation markers, it may be difficult to monitor membrane permeabilization via traditional fluorescence tags.[83] In this work, impedance-based monitoring systems are promising candidates used for observing membrane permeabilization because electrical properties are dominant in cell membranes.[66, 84] Thus, changes in membrane properties, i.e., electrical-signature variations, can be detected through impedance measurements, which is a long-recovery and low-bias-voltage method for membrane-permeabilization-monitoring.[85] In experiments, current systems with medium cell populations demonstrated an average recovery time of ~76 min (Supporting Fig. S6). In contrast, a recovery time of ~720 min is disclosed by the systems utilized in this work. Additionally, the system exhibited an increased conductance with an increase in number of pulses through weak-bias amplitudes, which has not been demonstrated before. Additionally, intermediate/ low cell viability for up to an average of ~66 pulses were shown by existing systems with medium cell populations (Supporting Fig. S8). On the other hand, the system harnessed in this work showed excellent cell viability for up to ~200 pulses. The all-atom MD simulations utilized in this work revealed an increase in degree of permeabilization driven by orientational disordering, which has not been reported before. In addition, for this work, a previously unreported flexibility of phospholipid headgroups upon the application of electric-field pulses was elucidated by simulations. Furthermore, state-of-the-art simulations showed the utilization of models with an average model size of ~240 lipids (Supporting Fig. S9). However,

the use of models with a model size of ~2000 lipids is described in the simulations harnessed in this work.

Recently, cancer studies have provided deeper insights into the dynamics of cancer invasion and metastasis.[86, 87] Studies have shown that cancer cells demonstrate collective migration and invasion, where cells migrate and invade surrounding tissues as a group (group of connected cells).[87] Understanding collective dynamics of cancer development can lead to new strategies for cancer monitoring, which implies that traditional single cell-based studies may not be sufficient.[37, 88, 89] As a result, utilizing medium cell populations can not only enhance understanding of cancer development, but also reduce intrinsic heterogeneity within the cell population.[90, 91] This would improve the reliability of results in applications such as drug development, tumor characterization and other biological studies.

Further studies can be performed to optimize system performance. Although membrane permeabilization may be enhanced by applying an increased number of pulses, the distributions of nanopores generated during electroporation are not uniform.[64, 92, 93] This is because a non-uniform electric-field distribution is created in the cells, leading to uneven distributions of pores formed on the membranes.[64, 92, 93] Moreover, distributions of pores formed for the homogenous-electric-field-distribution cases tends to be uneven due to the polarization of cells. [94, 95] The localized electric-fields in each region of cells can be different.[94, 95] As a result, structurally-different pores are formed in the cells.[96] Further investigations into the structure and dynamics of pores formed could open opportunities for optimizing monitoring-system performance.

Additionally, the utilization of biological assays such as Western blotting and polymerase chain reaction (PCR) in cells prior to and upon nanosecond electroporation would help to further clarify the mechanisms behind pore formation and cell toxicity. Experiments have demonstrated

that a signaling pathway associated with c-Jun N-terminal kinases (JNKs) is generated in HeLa S3 cells.[97] The JNKs activation occurs 30 min after nanosecond pulse electroporation, indicating that nanosecond electroporation could induce stress-associated responses. Moreover, different apoptosis mechanisms in cells were shown in experiments, due to the manipulation of electrical parameters in electroporation process, resulting in the optimization of nanosecond electroporation to achieve precise and targeted results.[98–100]

Conclusion

In conclusion, these long recovery times are achieved through an orientational disordering process in electroporation systems that modulates the membrane permeabilization of PANC-1 cells. We have created an electroporation system that utilizes few-volt nanosecond AC stimulation with increased number of pulses. This integration of increasing number of AC pulses and weak nanosecond stimulations can increase recovery time, opening the way to the realization of high-performance electroporation technologies for genetic engineering, gene therapy and molecular medicine.

References

[1] A. K. Chakka, M. S. Sriraksha, and C. N. Ravishankar. **(2021)**, *151,* 112140.

[2] J. Shi, Y. Ma, J. Zhu, Y. Chen, Y. Sun, Y. Yao, Z. Yang, and J. Xie. **(2018)**, *23,*.

[3] R. M. Brock, N. Beitel-White, R. V. Davalos, and I. C. Allen. *Front. Oncol.* **(2020)**, *10,* 1–9.

[4] C. Mansson, A. Nilson, P. Nygren, and B.-M. Karlson. *Anticancer Res.* **(2020)**, *40,* 2771–2775.

[5] M. Guo, J. Chen, X. Yun, K. Chen, L. Nie, and S. Yao. *Biochim. Biophys. Acta - Gen. Subj.* **(2006)**, *1760,* 432–439.

[6] D. Lee, S. S. Chan, N. Aksic, N. Bajalovic, and D. K. Loke. *ACS Omega* **(2021),** *6*, 35325–35333.

[7] Z. Xu, A. Patel, N. J. Tursi, X. Zhu, K. Muthumani, D. W. Kulp, and D. B. Weiner. *Front. Med. Technol.* **(2020)**, *0,* 5.

[8] P. Quaglino, C. Mortera, S. Osella-Abate, M. Barberis, M. Illengo, M. Rissone, P. Savoia, and M. G. Bernengo. *Ann. Surg. Oncol.* **(2008)**, *15,* 2215–2222.

[9] G. Pucihar, M. Pavlovec, S. Ribarič, M. Mali, A. Maček-Lebar, M. Petkovšek, J. Nastran, S. Kranjc, M. Čemažar, and G. Serša. **(2005)**, *65,* 121–128.

[10] T. García-Sánchez, B. Sánchez-Ortiz, I. Vila, M. Guitart, J. Rosell, A. M. Gómez-Foix, and R. Bragós. *J. Membr. Biol.* **(2012)**, *245,* 617–624.

[11] T. Forjanič and D. Miklavčič. *Biomed. Eng. Online* **(2018)**, *17,* 1–10.

[12] D. C. Chang, P. Q. Gao, and B. L. Maxwell. *BBA - Mol. Cell Res.* **(1991)**, *1092,* 153–160.

[13] C. Yao, Y. Lv, Y. Zhao, S. Dong, H. Liu, and J. Ma. *Sci. Rep.* **(2017)**, *7,* 1–16.

[14] M. B. Sano, C. B. Arena, M. R. DeWitt, D. Saur, and R. V. Davalos. **(2014)**, *100,* 69–79.

[15] S. J. Beebe, P. F. Blackmore, J. White, R. P. Joshi, and K. H. Schoenbach. *Physiol. Meas.* **(2004)**, *25,* 1077–1093.

[16] J. A. White, P. F. Blackmore, K. H. Schoenbach, and S. J. Beebe. *J. Biol. Chem.* **(2004)**, *279,* 22964–22972.

[17] P. Zhou, F. He, Y. Han, B. Liu, and S. Wei. **(2018)**, *124,* 7–12.

[18] I. Semenov, S. Xiao, O. N. Pakhomova, and A. G. Pakhomov. *Cell Calcium* **(2013)**, *54,* 145–150.

[19] S. J. Beebe, P. M. Fox, L. J. Rec, E. L. K. Willis, and K. H. Schoenbach. *FASEB J.* **(2003)**, *17,* 1493–1495.

[20] S. J. Beebe, P. M. Fox, L. J. Rec, K. Somers, R. H. Stark, and K. H. Schoenbach. *PPPS 2001 - Pulsed Power Plasma Sci. 2001* **(2015)**, *1,* 211–215.

[21] R. L. Vincelette, C. C. Roth, M. P. McConnell, J. A. Payne, H. T. Beier, and B. L. Ibey. *PLoS One* **(2013)**, *8,* 1–12.

[22] A. G. Pakhomov, J. F. Kolb, J. A. White, R. P. Joshi, S. Xiao, and K. H. Schoenbach. *Bioelectromagnetics* **(2007)**, *28,* 655–663.

[23] A. M. Bowman, O. M. Nesin, O. N. Pakhomova, and A. G. Pakhomov. *J. Membr. Biol.* **(2010)**, *236,* 15–26.

[24] O. M. Nesin, O. N. Pakhomova, S. Xiao, and A. G. Pakhomov. *Biochim. Biophys. Acta - Biomembr.* **(2011)**, *1808,* 792–801.

[25] A. G. Pakhomov, B. L. Ibey, A. M. Bowman, F. M. Andre, and O. N. Pakhomova. *IFMBE Proc.* **(2009)**, *25,* 17–20.

[26] A. G. Pakhomov, E. Gianulis, P. T. Vernier, I. Semenov, S. Xiao, and O. N. Pakhomova. *Biochim. Biophys. Acta - Biomembr.* **(2015)**, *1848,* 958–966.

[27] Y. Urano, D. Asanuma, Y. Hama, Y. Koyama, T. Barrett, M. Kamiya, T. Nagano, T. Watanabe, A. Hasegawa, P. L. Choyke, and H. Kobayashi. *Nat. Med.* **(2009)**, *15,* 104–109.

[28] M. Shi, K. Shen, B. Yang, P. Zhang, K. Lv, H. Qi, Y. Wang, M. Li, Q. Yuan, and Y. Zhang. *Theranostics* **(2021)**, *11,* 2349–2363.

[29] D. K. Loke, G. J. Clausen, J. F. Ohmura, T. C. Chong, and A. M. Belcher. *ACS Appl. Nano Mater.* **(2018),** *1*, 6556–6562.

[30] Z. Liu, X. Liang, H. Liu, Z. Wang, T. Jiang, Y. Cheng, M. Wu, D. Xiang, Z. Li, Z. L. Wang, and L. Li. *ACS Nano* **(2020)**, *14,* 15458–15467.

[31] A. Hai and M. E. Spira. *Lab Chip* **(2012)**, *12,* 2865–2873.

[32] V. Novickij, A. Zinkevičienė, V. Malyško, J. Novickij, J. Kulbacka, N. Rembialkowska, and I. Girkontaitė. *J. Photochem. Photobiol. B Biol.* **(2020)**, *213,* 112066.

[33] F. Shi, A. Steuer, J. Zhuang, and J. F. Kolb. *IEEE Trans. Biomed. Eng.* **(2019)**, *66,* 2010–2021.

[34] A. Vižintin, S. Marković, J. Ščančar, and D. Miklavčič. **(2021)**, *140,* 107798.

[35] D. Xiao, L. Tang, C. Zeng, J. Wang, X. Luo, C. Yao, and C. Sun. *Cell Biol. Int.* **(2011)**, *35,* 99–104.

[36] P. M. Graybill and R. V. Davalos. *Cancers (Basel).* **(2020)**, *12,* 29–32.

[37] L.-Y. Guan, J.-Q. Lv, D.-Q. Zhang, and B. Li. **(2021)**, *12,* 112.

[38] S. Chifflet and J. A. Hernández. *Int. J. Cell Biol.* **(2012)**, *2012,*.

[39] E. Sitarska and A. Diz-Muñoz. *Curr. Opin. Cell Biol.* **(2020)**, *66,* 11–18.

[40] C. Callies, J. Fels, I. Liashkovich, K. Kliche, P. Jeggle, K. Kusche-Vihrog, and H. Oberleithner. *J. Cell Sci.* **(2011)**, *124,* 1936–1942.

[41] H. B. Kim, S. Lee, J. H. Chung, S. N. Kim, C. K. Sung, and K. Y. Baik. *Appl. Biochem. Biotechnol.* **(2020)**, doi:10.1007/s12010-020-03271-4.

[42] L. Jaatinen, E. Young, J. Hyttinen, J. Vörös, T. Zambelli, and L. Demkó. *Biointerphases* **(2016)**, *11,* 011004.

[43] H. B. Kim, S. Lee, Y. Shen, P. D. Ryu, Y. Lee, J. H. Chung, C. K. Sung, and K. Y. Baik. *Biochem. Biophys. Res. Commun.* **(2019)**, *517,* 703–708.

[44] S. Jo, J. B. Lim, J. B. Klauda, and W. Im. *Biophys. J.* **(2009)**, *97,* 50–58.

[45] L. Li, A. M. Belcher, and D. K. Loke. *Nanoscale* **(2020),** *12*, 24214–24227.

S. Jo, T. Kim, V. G. Iyer, and W. Im. *J. Comput. Chem.* **(2008)**, *29,* 1859–1865.

[46] G. Shahane, W. Ding, M. Palaiokostas, and M. Orsi. *J. Mol. Model.* **(2019)**, *25,* 1–13.

[47] M. Klähn and M. Zacharias. *Phys. Chem. Chem. Phys.* **(2013)**, *15,* 14427–14441.

[48] W. L. Jorgensen, J. Chandrasekhar, J. D. Madura, R. W. Impey, and M. L. Klein. *J. Chem. Phys.* **(1998)**, *79,* 926.

[49] S. S. Y. Chan, Y. Sing Tan, K.-X. Wu, C. Cheung, and D. K. Loke. *ACS Appl. Bio Mater.* **(2018)**, *1,* 210–215.

[50] S. S. Y. Chan, D. Lee, M. P. Meivita, L. Li, Y. S. Tan, N. Bajalovic, and D. K. Loke. *Nanoscale Adv.* **(2021)**, doi:10.1039/D1NA00614B.

[51] M. J. Abraham, T. Murtola, R. Schulz, S. Páll, J. C. Smith, B. Hess, and E. Lindah. **(2015)**, *1–2,* 19–25.

[52] G. Bussi, D. Donadio, and M. Parrinello. *J. Chem. Phys.* **(2007)**, *126,* 014101.

[53] M. Parrinello and A. Rahman. *J. Appl. Phys.* **(1998)**, *52,* 7182.

[54] W. G. Hoover. *Phys. Rev. A* **(1985)**, *31,* 1695.

[55] S. Nosé. *J. Chem. Phys.* **(1998)**, *81,* 511.

[56] T. Darden, D. York, and L. Pedersen. *J. Chem. Phys.* **(1998)**, *98,* 10089.

[57] U. Essmann, L. Perera, M. L. Berkowitz, T. Darden, H. Lee, and L. G. Pedersen. *J. Chem. Phys.* **(1998)**, *103,* 8577.

[58] S. Miyamoto and P. A. Kollman. *J. Comput. Chem.* **(1992)**, *13,* 952–962.

[59] B. Hess, H. Bekker, H. J. C. Berendsen, and J. G. E. M. Fraaije. *J. Comput. Chem.* **(1997)**, *18,* 1463–1472.

[60] W. Humphrey, A. Dalke, and K. Schulten. *J. Mol. Graph.* **(1996)**, *14,* 33–38.

[61] W. J. Allen, J. A. Lemkul, and D. R. Bevan. *J. Comput. Chem.* **(2009)**, *30,* 1952–1958.

[62] Y. Atsmon-Raz and D. P. Tieleman. *J. Phys. Chem. B* **(2017)**, *121,* 11132–11143.

[63] S. Arasteh and M. Bagheri. *Methods Mol. Biol.* **(2017)**, *1548,* 103–118.

[64] P. Thomas Vernier, M. J. Ziegler, Y. Sun, M. A. Gundersen, and D. P. Tieleman. *Phys. Biol.* **(2006)**, *3,* 233–247.

[65] S. Hossain and A. Abdelgawad. *Electromagn. Biol. Med.* **(2020)**, *39,* 20–29.

[66] M. Al Ahmad, Z. Al Natour, F. Mustafa, and T. A. Rizvi. *IEEE Access* **(2018)**, *6,* 25979–25986.

[67] J. Teissie and T. Y. Tsong. *Biochemistry* **(2002)**, *20,* 1548–1554.

[68] U. Zimmermann, G. Pilwat, F. Beckers, and F. Riemann. *Bioelectrochemistry Bioenerg.* **(1976)**, *3,* 58–83.

[69] R. Sundararajan. **(Woodhead Publishing, 2014).**,.

[70] J. N. Sachs, H. Nanda, H. I. Petrache, and T. B. Woolf. *Biophys. J.* **(2004)**, *86,* 3772–3782.

[71] M. Kotulska, K. Kubica, S. Koronkiewicz, and S. Kalinowski. **(2007)**, *70,* 64–70.

[72] J. P. M. Jämbeck and A. P. Lyubartsev. *J. Chem. Theory Comput.* **(2012)**, *8,* 2938–2948.

[73] S. Moradi, A. Nowroozi, and M. Shahlaei. *RSC Adv.* **(2019)**, *9,* 4644–4658.

[74] J. P. M. Jämbeck and A. P. Lyubartsev. *J. Phys. Chem. B* **(2012)**, *116,* 3164–3179.

[75] T. J. Piggot, D. A. Holdbrook, and S. Khalid. *J. Phys. Chem. B* **(2011)**, *115,* 13381–13388.

[76] D. V. Zhelev and D. Needham. *BBA - Biomembr.* **(1993)**, *1147,* 89–104.

[77] E. Karatekin, O. Sandre, and F. Brochard-Wyart. *Polym. Int.* **(2003)**, *52,* 486–493.

[78] H. Isambert. *Phys. Rev. Lett.* **(1998)**, *80,* 3404–3407.

[79] J. C. Weaver and P. T. Vernier. **(2017)**, *0,* 1–6.

[80] X. Guo and R. Zhu. *Sci. Rep.* **(2016)**, *6,* 31392.

[81] M. Pavlin and D. Miklavčič. **(2008)**, *74,* 38–46.

[82] S. J. Beebe. **(Springer Singapore).**, doi:10.1007/978-981-10-5113-5.

[83] W. Bo, M. Silkunas, U. Mangalanathan, V. Novickij, M. Casciola, I. Semenov, S. Xiao, O. N. Pakhomova, and A. G. Pakhomov. *Int. J. Mol. Sci.* **(2020)**, *21,*.

[84] R. Binggeli and R. C. Weinstein. *J. Theor. Biol.* **(1986)**, *123,* 377–401.

[85] J. Hong, K. Kandasamy, M. Marimuthu, C. S. Choi, and S. Kim. *Analyst* **(2011)**, *136,* 237–245.

[86] T. Nagai, T. Ishikawa, Y. Minami, and M. Nishita. *J. Biochem.* **(2020)**, *167,* 347–355.

[87] T. S. Deisboeck and I. D. Couzin. **(2009)**, *31,* 190–197.

[88] E. M. Grasset, T. Bertero, A. Bozec, J. Friard, I. Bourget, S. Pisano, M. Lecacheur, M. Maiel, C. Bailleux, A. Emelyanov, M. Ilie, P. Hofman, G. Meneguzzi, C. Duranton, D. V. Bulavin, and C. Gaggioli. *Cancer Res.* **(2018)**, *78,* 5229–5242.

[89] P. Friedl and D. Gilmour. *Nat. Rev. Mol. Cell Biol.* **(2009)**, *10,* 445–457.

[90] S. Halldorsson, E. Lucumi, R. Gómez-Sjöberg, and R. M. T. Fleming. *Biosens.*

Bioelectron. **(2015)**, *63,* 218–231.

[91] G. C. Yuan, L. Cai, M. Elowitz, T. Enver, G. Fan, G. Guo, R. Irizarry, P. Kharchenko, J. Kim, S. Orkin, J. Quackenbush, A. Saadatpour, T. Schroeder, R. Shivdasani, and I. Tirosh. *Genome Biol.* **(2017)**, *18,* 1–8.

[92] M. J. Ziegler and P. Thomas Vernier. *J. Phys. Chem. B* **(2008)**, *112,* 13588–13596.

[93] D. C. Sweeney, M. Reberšek, J. Dermol, L. Rems, D. Miklavčič, and R. V. Davalos. *Biochim. Biophys. Acta - Biomembr.* **(2016)**, *1858,* 2689–2698.

[94] G. Saulis. *Food Eng. Rev. 2010 22* **(2010)**, *2,* 52–73.

[95] M. Leguèbe, A. Silve, L. M. Mir, and C. Poignard. *J. Theor. Biol.* **(2014)**, *360,* 83–94.

[96] E. Tekle, R. D. Astumian, W. A. Friauf, and P. B. Chock. *Biophys. J.* **(2001)**, *81,* 960–968.

[97] K. Morotomi-Yano, Y. Uemura, S. Katsuki, H. Akiyama, and K. ichi Yano. *Biochem. Biophys. Res. Commun.* **(2011)**, *408,* 471–476.

[98] H. Zhang, K. Liu, Z. Xue, H. Yin, H. Dong, W. Jin, X. Shi, H. Wang, and H. Wang. *Am. J. Transl. Res.* **(2018)**, *10,* 334–351.

[99] Z. Xiong, C. Yao, W. Zhou, Y. Liu, and C. Li. *J. Cancer Res. Ther.* **(2012)**, *8,* 80.

[100] X. Chen, J. F. Kolb, R. J. Swanson, K. H. Schoenbach, and S. J. Beebe. *Pigment Cell Melanoma Res.* **(2010)**, *23,* 554–563.

Acknowledgments. We thank K.G. Lim, L.T. Ng, A.H. Firdaus and J.Y. Koh for important discussions. The authors acknowledge support from the Singapore University of Technology and Design (SUTDT12017003), Changi General Hospital (Singapore) (CGH-SUTD-HTIF2019-001), Ministry of Education (Singapore) (MOE-T2EP50220-0022), SUTD-Zhejiang-University

(SUTD-ZJU (VP) 201903), and Agency of Science Technology and Research (Singapore) (A20G9b0135) grant programs. D.K.L. acknowledges support from the Massachusetts Institute of Technology–SUTD International Design Centre and National Supercomputing Centre, Singapore (15001618). D. L. acknowledges support from the SUTD President Graduate Scholarship.

Data availability. The authors declare that data supporting the finding of this study are available within the article and the Supporting Information. Other data are available from the corresponding authors upon reasonable request.

Competing interests. The authors declare no competing interests.

Keywords. Cancer cells, molecular dynamics simulations, electroporation, monitoring, nanosecond-scale